ACS APPLIED ELECTRONIC MATERIALS

Open Access

This article is licensed under CC-BY 4.0

pubs.acs.org/acsaelm

Article

# Neutron Detection with Isotopically Enriched Boron Carbide Thin Layers Combined with an Oxygen Vacancy-Enriched Sapphire Scintillator

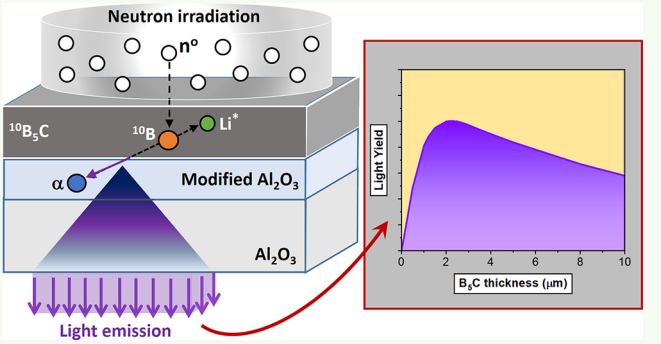
Zsolt Zolnai,* Zoltán Kis, Nguyen Quoc Khánh, Zoltán Kovács, Péter Petrik, Chao Zeng, Edit Szilágyi, Attila Németh, László Szentmiklósi, and János Volk

Cite This: *ACS Appl. Electron. Mater.* 2026, 8, 8664–8672

Read Online

ACCESS | Metrics & More | Article Recommendations | Supporting Information

**ABSTRACT:** Isotopically enriched $^{10}B_5C$ neutron absorber layers were combined with α-$Al_2O_3$ crystals to achieve scintillation-based neutron detection, utilizing the $^{10}B(n,\alpha)^7Li$ nuclear reaction and ionoluminescence induced by the stopping of secondary charged particles as reaction products. The thin $^{10}B_5C$ layers were deposited by DC magnetron sputtering on Si wafers. The modified near-surface region of α-$Al_2O_3$ contained excess oxygen vacancy-related optical centers to enhance the ionoluminescence yield in the scintillator. Neutron absorption and neutron irradiation-induced scintillation measurements were performed with cold neutrons of a 3.4 Å average wavelength. Measured and calculated values agree well for neutron absorption vs the areal density of deposited $^{10}B$ atoms. The maximum neutron-to-light conversion efficiency was found at ~20% neutron absorption for a $^{10}B_5C$ layer of 2.5 μm thickness. The measured and calculated relative scintillation yields agree well and show that the maximum neutron detection efficiency is determined by the total amount of ionization energy deposited in $Al_2O_3$. The net scintillation light yield is a result of the interplay between neutron absorption in $^{10}B_5C$ and the degree of penetration of the nuclear reaction products into $Al_2O_3$. The ionization profiles induced in $Al_2O_3$ are confined to the $^{10}B_5C/Al_2O_3$ interface; therefore, it is enough to sensitize only a thin surface region of the scintillator to achieve significant enhancement in neutron detection efficiency. This work assigns $^{10}B_5C$ as an effective neutron absorber material for small-scale compact solid state neutron detectors with a wide range of possible applications.




**KEYWORDS:** *boron carbide, sapphire, oxygen vacancy, neutron absorption, scintillation, ionoluminescence*

## 1. INTRODUCTION

Neutrons as effective characterization tools are utilized in a wide range of materials research issues,[1−4] but they also appear as byproducts, e.g., in fusion-based energy production or semiconductor industry. Recently, multi-blade neutron detectors were developed at ESS for neutron reflectometry measurements,[5] while a neutron-based recoil spectrometer has been introduced for ITER plasma diagnostics.[6] Moreover, neutron radiation is a safety concern in semiconductor processing for high energy ion implanters when certain ion-target collisions during implantation of light species, e.g. $H^+$ and $B^+$, result in considerable neutron generation.[7,8] In this case, neutron detectors and shielding materials have to be applied to control radiation exposure in accordance with safety limits.

Beyond fundamental research and industrial aspects, there is a demand for the environmental monitoring of neutrons. The effect of hydrogen surroundings on the energy spectra of neutrons originating from secondary cosmic radiation enables soil moisture monitoring in agriculture[9] or the measure of snow cover at mountain altitudes.[10] Further issues are thunderstorm monitoring via neutron burst detection during lightning,[11,12] utilization of the response of thermalized neutrons to geodynamic phenomena like earthquakes,[13] or monitoring the moderation of cosmic-ray generated neutrons by water deposits on the Moon's surface.[14]

New demands in a wide range of such applications call for continuous development of novel materials and versatile integrable neutron detector structures on the micron scale. In this progress, compact solid state detectors may be superior to those containing liquid or gaseous components.[15−17] Recently, the global shortage

**Received:** July 13, 2026
**Revised:** September 14, 2026
**Accepted:** September 14, 2026
**Published:** September 21, 2026



Downloaded from pubs.acs.org/aaemdp/article-pdf/8/19/8664/6858615/el-2026-01505k.pdf by CENTER FOR ENERGY RESEARCH user on 06 November 2026



© 2026 The Author(s). Published by American Chemical Society

of $^3$He resources[15,17] induced the development of $^3$He-free neutron detectors with a $^{10}$B-, $^6$Li-, or Gd-based absorber; however, $^{10}$B offers a promising alternative to the competitors. For instance, its thermal neutron capture cross section is 4 times higher than that of $^6$Li.[18] The products of the $^{10}$B(n,α)$^7$Li nuclear reaction have less total energy (2.31 or 2.79 MeV) than those of $^6$Li (4.78 MeV) and Gd (7.937 or 8.536 MeV).[18] Accordingly, shorter stopping ranges of the reaction products in $^{10}$B-based detector materials significantly reduce the required volume for neutron-to-photon[18,19] or neutron-to-charge carrier conversion.[20−22] Such characteristic pixel size reduction improves the spatial resolution in $^{10}$B-based neutron detectors and enables the downscale of active layer dimensions. A promising boron-containing material with unique physical properties is boron carbide, $B_4C$.[23] The stability of isotopically enriched $^{10}B_4C$ thin films under neutron radiation was demonstrated.[24] The high melting point (∼2450 °C) and thermal stability enable its use as a refractory material. It is also applied as an abrasive powder and coating and can be utilized in ballistic and space performance due to its low density and high hardness. Boron carbide is chemically inert, and its crystalline form is a high-temperature semiconductor, a potential candidate for novel electronic applications.[25]

Recently, various $^{10}$B thin layer-based thermal neutron detector structures were tested, which utilize gas containing charged particle energy converters, like multiwire proportional chambers and gas electron multipliers,[5,15,26] or apply solid state charge collection devices, e.g., GaAs diodes.[20,21] Also, several calculations were performed to optimize the thickness of the $^{10}$B or $^{10}B_4C$ film and the connected charge collection layer in α-voltaic thermal neutron detectors for best efficiency and γ-background rejection capability.[20,21,27,28] However, less attention was paid to systematic experimental testing of scintillation-based solid state coplanar detectors,[18,19,29,30] especially for a $^{10}$B-enriched $^{10}B_4C$ absorber, to optimize neutron-to-photon conversion efficiency while comparing experimental results with calculations. In such devices, the scintillator converts the kinetic energy of charged particles (primarily 1.47 MeV He and 0.84 MeV Li ions) to photons to be detected. $Al_2O_3$ is a promising scintillator material with favorable technological and structural properties, like scratch resistance, mechanical rigidity, chemical inertness, and radiation resistance, which makes it a potential candidate for long-term operation in harsh environments. In addition, appropriate defect engineering or doping can significantly enhance ionoluminescence-induced light emission, i.e., the scintillation yield of sapphire crystals.[31−34] In this work, we prepare compact, versatile $^{10}B_4C/Al_2O_3$ absorber/scintillator structures for neutron detection and perform systematical experiments to determine the optimal device thickness and scintillator properties for maximal light yield, i.e., ionoluminescence intensity. Measured light yields are compared to the results of model calculations for the neutron-to-light conversion efficiency. This procedure is based on the known energy spectrum of the incoming neutron beam, the detailed characterization of the $^{10}B_4C/Al_2O_3$ structure, and the well-established description of the neutron-to-photon conversion and optical detection processes in this system. It is found that sensitization of only a few microns-thick surface region of the scintillator is enough to enhance the neutron-induced light yield significantly.

## 2. EXPERIMENTAL SECTION

Boron carbide layer deposition was performed in a DC magnetron sputtering system (VAKSIS, MiDAS). Four inch ⟨100⟩ p-doped Si wafers with a thickness of 525 μm have been used as substrates. They were ultrasonically cleaned step-wise in acetone, ethanol, and deionized water for 5 min and purged in a nitrogen atmosphere. Then, the wafer was loaded into the sputtering chamber where the base pressure was in the range of $1 \times 10^{-5}$ to $1.6 \times 10^{-5}$ Pa. The substrate was further cleaned by RF plasma for 5 min using a 50 W input power under 5 mTorr high-purity argon (5 N) gas pressure. First, a thin Ti layer of ca. 9 nm thickness was deposited to enhance the adhesion of the boron carbide layer to the substrate. The boron carbide films were deposited by 250 W DC magnetron sputtering at room temperature. The working pressure was 7 mTorr to keep the mechanical strain in the layer at a low level. The Ar gas flow was 120 sccm. The sputtering cathode was a 3″ diameter × 3 mm thickness size, pure, isotopically enriched $^{10}B_4C$ disc target (from RHP-Technology GmbH), which was continuously water-cooled. A throttle valve between the vacuum pump and the main chamber was used to automatically keep the set gas pressure. During deposition, the substrate was rotated at 10 rpm to ensure film uniformity. The deposited boron carbide layer thickness varied in the range from ∼0.5 to ∼5 μm and was controlled by sputtering time. The atomic composition of the sputtered layers was found to be $\approx B_5C$. Using a shadow mask during successive deposition steps, $B_5C$ films with different thicknesses can be produced on a single Si wafer. The samples prepared by this procedure have a $Si/Ti/(B_5C/Ti)_n$, $n \geq 1$ stack structure, where the thin Ti top layer prevents oxidation of the topmost $B_5C$ layer. Another set of samples has a simple layer structure of $Si/Ti/B_5C$, without a Ti top layer, allowing the optical characterization of the boron carbide film. After the sputtering process, about 1 cm × 1.5 cm pieces were sliced from the full wafers by an automatic dicing saw.

Samples of about 1 cm × 1.5 cm size were cut from 4 inch *c*-plane α-$Al_2O_3$ wafers (thickness 650 μm, double-side polished, purity 99.998%, from Siegert Wafer GmbH). The $Al_2O_3$ scintillator layers were produced by the modification of their near-surface optical properties, i.e., generation of optically active defect centers in the topmost 2 μm region with MeV energy $N^+$ ion irradiation. Two single-energy implants were performed with 2.8 MeV energy $N^+$ ions to fluences of $5 \times 10^{13}$ and $5 \times 10^{14}$ cm$^{-2}$, and two triple-energy implants were carried out with energies of 0.8/1.8/2.8 MeV to fluences of $5 \times 10^{13}/5 \times 10^{13}/6.2 \times 10^{13}$ and $5 \times 10^{14}/5 \times 10^{14}/6.2 \times 10^{14}$ cm$^{-2}$. Applying 1.5 MeV $He^+$ ion beam-induced luminescence (IL), we previously identified two prominent emission bands in the IL spectra of $N^+$ irradiated samples, the well-known F and $F^+$ centers.[32−34] They are related to oxygen vacancy defects with different charge states, and their emission peaks appear in the UV-visible wavelength range at λ = 415 nm (F) and λ = 329 nm ($F^+$). More details on $Al_2O_3$ sample preparation and the IL method can be found in the Supporting Information and in our previous works.[32,35]

Elastic backscattering spectrometry experiments with protons (p-EBS) of 1.6 MeV energy were performed at the 5 MV Van de Graaff accelerator of the HUN-REN Wigner Research Centre for Physics in Budapest. The pressure in the scattering chamber and the measurement beam current were $1.8 \times 10^{-4}$ Pa and ∼10 nA (measured by a transmission Faraday cup[36]), while the beam spot size and divergence were 0.5 mm × 0.5 mm and 0.06°, respectively. Backscattered protons were detected by an ORTEC surface barrier detector mounted in Cornell geometry at a scattering angle of θ = 165°. The p-EBS spectra were recorded at two different sample tilt angles of 7° and 60° (measured between the sample normal and beam direction) to increase the accuracy of atomic compositional and thickness analysis for the boron carbide layers. Spectrum evaluation was performed with the RBX code.[37] Note that considerably enhanced non-Rutherford elastic backscattering cross sections appear for the $^{12}$C(p,p)$^{12}$C, $^{13}$C(p,p)$^{13}$C, and $^{10}$B(p,p)$^{10}$B reactions for proton energies around 1.6 MeV.[38−40] Such sensitivity enables to determine the $^{10}$B/C ratio in the boron carbide layers with good accuracy. Previously, our group demonstrated the strength of ion beam techniques in compositional and structural analysis of various thin layer structures.[41−47]

The thickness and morphology of the boron carbide layers were determined by field emission scanning electron microscopy (SEM) using a Zeiss LEO 1540 XB microscope.

Downloaded from pubs.acs.org/aaembp/article-pdf/8/19/8664/6858615/el-2026-01505k.pdf by CENTER FOR ENERGY RESEARCH user on 06 November 2026



https://doi.org/10.1021/acsaelm.6c01505
ACS Appl. Electron. Mater. 2026, 8, 8664−8672

The layer thickness and dielectric function for boron carbide were measured by a Woollam M-2000DI spectroscopic ellipsometer in the wavelength range of 250–1700 nm at angles of incidence of 65°, 70°, and 75°. The sample was described by an optical model that consists of a Si substrate covered by an adhesion Ti layer and a boron carbide layer on top (Si/Ti/$B_5C$ structure) with surface roughness.

Neutron absorption and scintillation light yield measurements were carried out at the NORMA (Neutron Optics and Radiography for Material Analysis) Cold Neutron Beam Imaging Station[48,49] operating at the Budapest Neutron Centre (BNC). At the facility, the average wavelength of incoming neutrons is 3.4 Å, and the maximum thermal equivalent neutron flux at the center of the beam is $2.7 \times 10^7$ $cm^{-2}s^{-1}$.[48] Further details on the measurement station and the neutron spectrum can be found elsewhere.[48,49] In neutron absorption measurements, neutrons transmitted through the boron carbide layers were detected by a 100 μm-thick green light-emitting $^6$LiF/ZnS:Cu (mixture 1:2) scintillation screen. The emitted photons were transmitted by a 45° mirror that reflects the light onto an imaging digital CCD camera module (Andor iKon-M 934) through a lens oriented perpendicular to the neutron beam. In this way, the $^6$LiF/ZnS:Cu scintillation screen converts the neutron transmission image of the sample into a visible light intensity map. In absorption measurements, the sample to screen distance was set to 11 cm, and the sample was attached by thin Teflon strings to a standing ∼10 cm × 10 cm size rectangular aluminum frame rotatable around its vertical axis. The acquisition of an image was performed with 12 s neutron exposure time, and such measurement cycle was repeated 10 times for each sample.

The $^{10}$B(n,α)$^7$Li nuclear reaction-induced scintillation light yield measurements were performed on the Si/Ti/$^{10}B_5C/Al_2O_3$- and Si/Ti/$(B_5C/Ti)_n/Al_2O_3$-type substrate/absorber/scintillator structures. In this case, the light source was the sample itself and the emitted photons were detected with the CCD camera, which enables a 32 × 32 binning of the pixels to achieve good light yield statistics from the area of the scintillation screen seen by an effective pixel (832 μm × 832 μm calculated with a native pixel size of 13 μm and an optical magnification of 0.5). In light yield measurements, the sample was fixed to a standing 25 mm × 25 mm × 1 mm size aluminum plate sample holder by Teflon tape and was put close to the focusing optics, which collects the incoming light in front of the 45° mirror. The sample and the optical detection path were prevented from undesired external light sources by appropriate shielding. Light yield experiments were performed with 30 s neutron exposition time, and such a measurement cycle was repeated three times for each sample.

Despite the potential of boron carbide, in this work, it was less preferred to achieve maximum spatial resolution for neutron detection. Instead, the $^{10}B_5C$ thickness dependence of neutron absorption and neutron-induced light emission as well as the effect of the near-surface optical defect concentration in $Al_2O_3$ was analyzed while ensuring low statistical uncertainty for the comparative light yield measurements. For the stationary neutron flux and applied fluence levels, such reliability enhancement can be achieved by the binning process, i.e., the choice of a larger effective pixel size and higher neutron-induced light yield per pixel. Further efforts are required to elucidate the trade-off between spatial resolution and reliable light yield measurement for a single pixel.

## 3. RESULTS AND DISCUSSION

Figure 1a shows the 1.6 MeV p-EBS spectra of Si/Ti/$(^{10}B_{5.2}C/Ti)_n$ layered samples ($n$ = 1, 2, and 3) for a 7° tilt angle. The energy of the backscattered protons depends on the collision kinematics (increasing proton backscattering energy with increasing mass of the scatterer target nuclei) and the energy losses in the sample (increasing proton energy loss with increasing depth, starting from the sample surface). The height of the spectrum depends on the amount and nuclear scattering cross section of the given target element. The whole spectrum can be composed from the sub-spectra of different elements in the sample.[37,50] For the thinnest (1.2 μm) $^{10}B_{5.2}C$ layer, spectrum edges for $^{10}$B, C, Si, and Ti (the top layer) are marked by arrows. All the small narrow peaks between channel numbers 390 and 500 mark thin Ti layers located on top (at channel no. ∼500) and below or embedded in the $^{10}B_{5.2}C$ layers of different thicknesses. The thicker the $^{10}B_{5.2}C$ layer above Ti, the more shifted the Ti peak is to lower channels. Also, the Si-related edge is shifted, from channel nos. 440 to 320, as the boron carbide layer thickness increases from 1.2 to 4.8 μm. Utilizing non-Rutherford cross sections in the proton elastic scattering of $^{10}$B and C (ca. 6- and 9-fold enhancements with respect to the Rutherford value), both components of boron carbide can be detected with sufficiently high intensity on the Si background. It was found that at a 7° sample tilt, above a boron carbide thickness of ∼0.9 μm, the $^{10}$B and C spectra start to overlap. Figure 1b shows the p-EBS spectrum of a Si/Ti/$^{10}B_{5.2}C$-type sample together with its RBX simulation represented by the solid line. The small peak at the O marker shows the presence of a thin $SiO_2$ layer on top of the Si substrate. A $^{10}B_{5.2}C$ atomic composition was derived from RBX spectrum simulations for the boron carbide layers. However, in this work (except for Figure 1 and few cases in this paragraph), we mark the boron carbide composition as $^{10}B_5C$ for simplicity. Similarly to that seen in Figure 1, p-EBS analysis

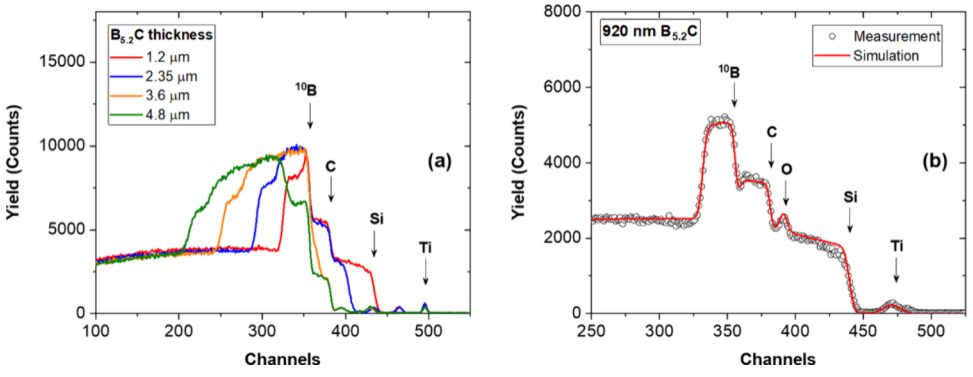



**Figure 1.** Sample 1.6 MeV p-EBS spectra of (a) Si/Ti/$(^{10}B_{5.2}C/Ti)_n$ structures with different total $^{10}B_{5.2}C$ thicknesses and (b) Si/Ti/$^{10}B_{5.2}C$-type sample with a $^{10}B_{5.2}C$ thickness of 920 nm together with its RBX simulation. Spectrum edges for Ti, Si, O, C, and $^{10}$B are indicated by arrows. For more details, see the text.



https://doi.org/10.1021/acsaelm.6c01505
ACS Appl. Electron. Mater. 2026, 8, 8664−8672

Downloaded from pubs.acs.org/aaembp/article-pdf/8/19/8664/6858615/el-2026-01505k.pdf by CENTER FOR ENERGY RESEARCH user on 06 November 2026

shows homogeneous depth distribution of the $^{10}B$ and C components in the boron carbide layers used in this work. The $^{10}B_{5.2}C$ layer thicknesses in units of atoms cm$^{-2}$ were also determined with good accuracy from RBX simulations of the spectra recorded at 7° and 60° tilt angles. The derived p-EBS thicknesses are given in Figure S1 (Supporting Information).

Figure 2 shows SEM cross-sectional micrographs of Si/Ti/$(^{10}B_5C/Ti)_n$ layered structures ($n$ = 1, 2, and 3) deposited on different segments of the Si wafer by DC sputtering combined with the shadow mask technique. The bright vertical stripes are the thin Ti layers located on top, below, or embedded in the $B_5C$ film. They can be clearly identified (due to the $Z$-contrast in SEM for Ti and $B_5C$) in good agreement with the Ti-related narrow peaks detected in the p-EBS spectra of the same samples (see Figure 1a). For each $B_5C$ layer, good thickness homogeneity and a vertical columnar layer structure can be observed. The layer thicknesses were estimated from SEM analysis, while the numbers of $^{10}B$ and C atoms in the layers were evaluated from p-EBS spectra. Strong linear correlation was found between the thicknesses provided by the two methods, see Figure S1. From the slope in Figure S1, the derived atomic density for the boron carbide layers is $1.22 \times 10^{23}$ cm$^{-3}$. This value is about 10% lower compared to that of $^{nat}B_4C$, i.e., $1.37 \times 10^{23}$ cm$^{-3}$, for a density of 2.52 g cm$^{-3}$ (2.37 g cm$^{-3}$ for $^{10}B_4C$).[23] However, our boron carbide layers show an amorphous structure and an excess boron content compared to the $B_4C$ structure, as it was discussed in the previous paragraph.

Figure 3 shows transmitted neutron intensity maps for Si/Ti/$^{10}B_5C$ layered samples with three different $^{10}B_5C$ thicknesses (determined by SEM)—appearing as light intensity maps of the $^6$LiF/ZnS:Cu scintillation screen recorded by the CCD camera. The response of the screen is determined by the number and energy distribution of neutrons transmitted through the Si/Ti/$^{10}B_5C$ samples[49] and, accordingly, the absorption efficiency of the screen for the transmitted neutrons. The experiments were performed at sample tilt angles of 0° and 60°, measured between the sample normal and the direction of the neutron beam. Lower brightness reveals lower neutron transmission, i.e., higher neutron absorption in the sample. As expected, neutron transmission is reduced more for thicker boron carbide layers and for 60° tilt as the effective $^{10}B_5C$ thickness is doubled for 60° tilting.

Figure 4 shows neutron absorption values as a function of $^{10}B$ thickness (in units of $^{10}B$ atoms/cm$^2$) evaluated from light

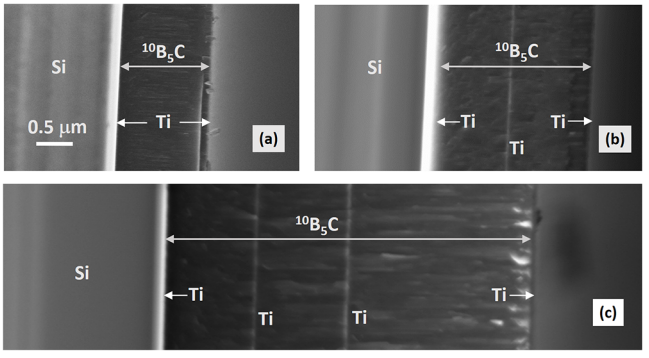



**Figure 2.** SEM cross-sectional micrographs of Si/Ti/$(^{10}B_5C/Ti)_n$ structures with total $^{10}B_5C$ thickness of (a) 1.2 μm, (b) 2.35 μm, and (c) 4.8 μm. The thin Ti layers, located on top, below, or embedded in the $B_5C$ films, are also indicated.

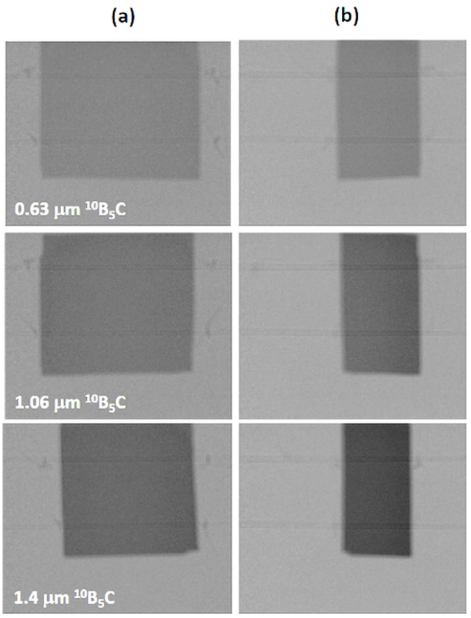



**Figure 3.** Neutron transmission images of isotopically enriched $^{10}B_5C$ layers with different thicknesses measured for sample tilt angles of (a) 0° and (b) 60°. The higher the neutron absorption, the darker the image of the absorber layer. Thin horizontal darker lines are the projected images of the Teflon strings.

yield maps of the $^6$LiF/ZnS:Cu screen. Data evaluation was performed after flat-field correction and appropriate background (i.e., camera dark current) subtraction for the collected light maps. Considering measurement statistics, the estimated experimental errors are comparable or even smaller than the symbol size. Dashed lines show calculated absorption values for boron carbide layers considering the NORMA neutron energy spectrum[49] (with $^{10}B$ absorption cross sections according to the $\sim 1/v$ rule, where $v$ is the neutron velocity) and effective $^{10}B$ thicknesses evaluated from p-EBS spectra. This estimation results in somewhat lower values than the experimental data. The agreement is better for the solid lines calculated by taking into account additional effects, like Si substrate-related neutron attenuation, and the finite size effect on the neutron absorption, thus the scintillation response of the 100 μm-thick $^6$LiF/ZnS:Cu screen. Linear dependence of the ZnS:Cu light yield on the number of neutrons absorbed by $^6$Li atoms was assumed. In all calculations, neutron scattering by $^{10}B$ and carbon atoms was neglected due to the low cross sections[51] for these processes compared to the absorption cross section of $^{10}B$ (3836 barn for thermal neutrons). Calculations show ~1.1% and ~2.2% attenuation for NORMA neutrons due to absorption and scattering by the Si substrate[51] at 0° and 60° sample tilt angles, respectively. These values are comparable to the measured ones, that is, ~0.98% and ~1.12%. Neutron transmission images for the bare Si substrate and the bare $Al_2O_3$ scintillator are shown in Figure S2.

As shown in Figure 4, the $^{10}B_5C$ layers are efficient cold neutron absorbers since a thickness of ~3 μm (~$3 \times 10^{19}$ cm$^{-2}$ for $^{10}B$) is enough to reach ~20% absorption of NORMA neutrons. Further increasing the amount of $^{10}B$ results in about 50% absorption for an ~5 μm-thick layer tilted off by 60° (i.e., for an effective $^{10}B$ thickness of ~$10^{20}$ cm$^{-2}$). Note that the absorption of the 100 μm-thick $^6$LiF/ZnS:Cu screen for

Downloaded from pubs.acs.org/aaembp/article-pdf/8/19/8664/6858615/el-2026-01505k.pdf by CENTER FOR ENERGY RESEARCH user on 06 November 2026



https://doi.org/10.1021/acsaelm.6c01505
ACS Appl. Electron. Mater. 2026, 8, 8664−8672

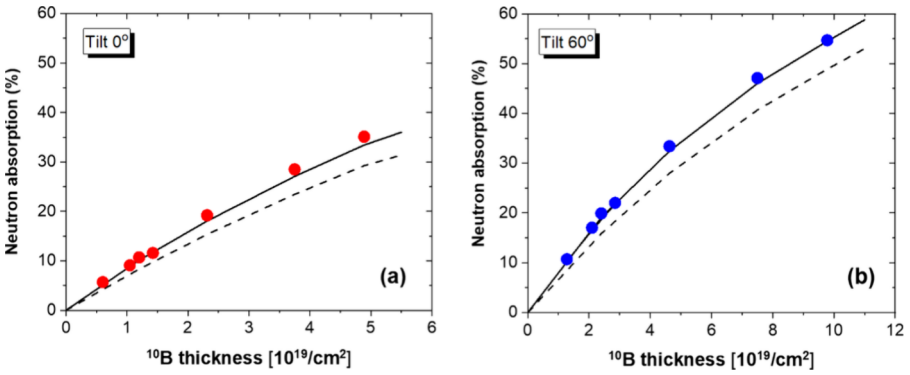



**Figure 4.** Neutron absorption as a function of effective $^{10}$B thickness for isotopically enriched $^{10}B_5C$ layers deposited on the Si substrate, measured at (a) 0° and (b) 60° sample tilt angles with respect to the neutron beam. Symbols: measurement, dashed line: calculation considering the $^{10}B_5C$ absorption effect only, solid line: calculation considering $^{10}B_5C$-related neutron absorption, Si substrate-related neutron attenuation, and neutron absorption/conversion in the $^6$LiF/ZnS:Cu scintillation screen. Neutron energy dependence for these processes was also considered.

NORMA neutrons is ~24%. These experiments show that thin $^{10}$B containing layers, like $^{10}B_5C$, are suitable for effective shielding against low energy neutrons. Indeed, a recent study confirms the superior attenuation properties of $B_4C$ modified concrete allowing for use in nuclear, medical, and other facilities requiring radiation shielding.[52]

In Figure 5a, neutron irradiation-induced normalized light yields of Si/Ti/($^{10}B_5C$/Ti)$_n$/$Al_2O_3$-type substrate/absorber/scintillator structures are shown as a function of the total $^{10}B_5C$ layer thickness. Red and blue symbols represent measured data for two α-$Al_2O_3$ scintillators with lower and higher amounts of oxygen vacancy-related F and $F^+$ optical centers in their 2 μm-thick near-surface region (the "modified $Al_2O_3$" zone in Figure 6), respectively. The estimated experimental errors are comparable to the symbol size. In Figure 5a, the calculated (dashed lines) and measured data agree well, thus showing a maximum light yield at a $^{10}B_5C$ thickness of ~2.5 μm. Below this value, the neutron absorption decrease (Figure 4) dominates, while for thicker $^{10}B_5C$ layers, the determining factor is the probability of α- and Li-particle escape from $B_5C$ that reduces the same as the fraction of ionization energy deposited in $Al_2O_3$ and the neutron-to-light conversion efficiency. Note that the thickness dependence is dominated by the prevalent 94% branch of the nuclear reaction, i.e., the $^{10}$B(n,αγ)$^7$Li$^*$ process, with $Q$ = 2.31 MeV (1.47 MeV α-products and 0.84 MeV Li-products, 470 keV γ-photon emission). The effect of the weak 6% reaction branch with $Q$ = 2.79 MeV (1.78 MeV α-products and 1.01 MeV Li-products, no γ-photon emission) is small on the thickness dependence of the light yield. In both $B_5C$ and $Al_2O_3$, the stopping ranges and electronic stopping profiles are quite different for the Li- and α-particles, see Figure S3a in the Supporting Information. Accordingly, the optimal $B_5C$ thicknesses for the maximum IL yield in $Al_2O_3$ differ too, as they appear at ~1.5 μm for Li and ~2.5 μm for α, see Figure S3c. Since α-particles deposit about 4 times higher ionization energy in $Al_2O_3$ than Li-projectiles, see Figure S3b,c, the $B_5C$ thickness dependence of the IL yield may be dominated by α-stopping. Indeed, this expectation is confirmed by the experimental results in Figure 5a.

For the two $Al_2O_3$ scintillators (red and blue colors) in Figure 5a, similar $^{10}B_5C$ thickness dependence can be observed, but their relative light yields differ by about 25%. This effect is more accentuated in Figure 5b, where neutron-induced light yields of Si/Ti/($^{10}B_5C$/Ti)$_n$/$Al_2O_3$ ($n$ = 2) structures with a fixed $^{10}B_5C$ thickness of 3.6 μm are represented. Here, the normalized light yield is shown as a function of areal density of excess oxygen vacancies (estimated from SRIM[53] simulations) formed in the modified $Al_2O_3$ region. The decreasing IL yield

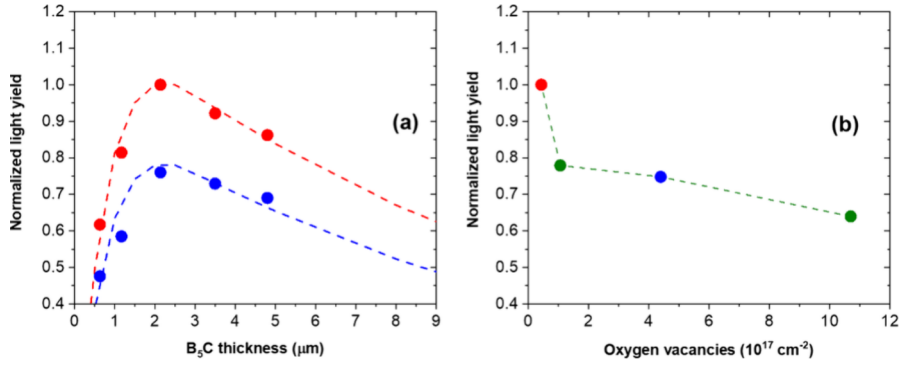



**Figure 5.** Normalized neutron irradiation-induced light yield of Si/Ti/($^{10}B_5C$/Ti)$_n$/$Al_2O_3$ layered substrate/absorber/scintillator structures as a function of (a) total $^{10}B_5C$ layer thickness; (b) areal density of oxygen vacancies in $Al_2O_3$, for a fixed $^{10}B_5C$ thickness of 3.6 μm. In panel (a), dots show measured values while dashed lines indicate calculations. Red and blue colors represent two different oxygen vacancy contents in $Al_2O_3$. In panel (b), the dashed line is only to guide the eye while the red and blue dots mark the $Al_2O_3$ scintillators used in the experiments shown in panel (a).



https://doi.org/10.1021/acsaelm.6c01505
ACS Appl. Electron. Mater. 2026, 8, 8664−8672

Downloaded from pubs.acs.org/aaembp/article-pdf/8/19/8664/6858615/el-2026-01505k.pdf by CENTER FOR ENERGY RESEARCH user on 06 November 2026

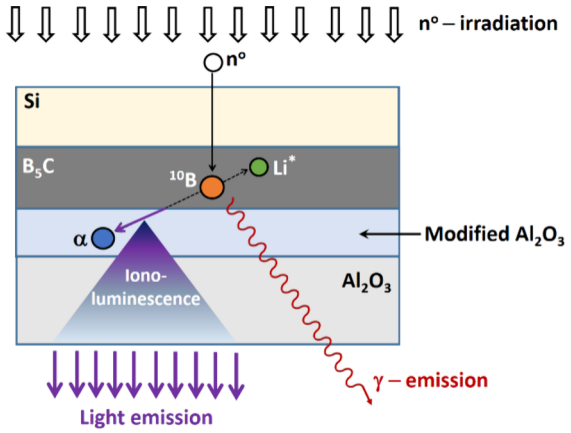



**Figure 6.** Schematic representation of neutron irradiation-induced ionoluminescence and γ-ray emission from a $Si/^{10}B_5C/Al_2O_3$ structure.

for increasing amount of defects is understood from Figure S4 that shows 1.5 MeV $He^+$ ion beam-induced IL yields for the same set of $Al_2O_3$ samples shown in Figure 5b. In the IL measurements shown in Figure S4, the MeV energy α-particles were not received from the $^{10}B(n,\alpha\gamma)^7Li^*$ nuclear reaction but were produced by a high voltage ion beam accelerator.[32] In this case, the IL peak intensities were determined separately for the F and $F^+$ centers from the measured spectra. As a result, different IL yield changes, i.e., a maximum-like behavior and a monotonous decrease, can be observed for the F and $F^+$ centers, respectively. Considering that in NORMA measurements, the integrated light yield is recorded by the CCD without wavelength separation, the neutron irradiation-induced IL emission in Figure 5b seems to be dominated by the F center. This effect can primarily be attributed to the fact that the quantum efficiencies (QEs) of the CCD camera at the NORMA station are ca. 10% and 65% at the emission wavelengths of the $F^+$ and F centers, respectively. Note that the QE of this camera is optimized for standard neutron radiography measurements performed with the green-light-emitting $^6LiF/ZnS:Cu$ screen. We intend to perform further experiments at NORMA with an optical detector of high sensitivity for both the F and $F^+$ centers.

As shown in Figure S4, an excess oxygen vacancy content of $\sim 4 \times 10^{16}$ $cm^{-2}$ in $Al_2O_3$ is enough to enhance the $He^+$-induced IL yield with respect to the reference sample (without $N^+$ pre-implantation). Moreover, the ionization profiles in Figure S3b confirm that it is sufficient to sensitize only a 2 μm-thick near-surface region of the scintillator to achieve a remarkable increase in neutron-to-light conversion efficiency. While our results are obtained for a cold neutron source, many experiments and calculations in the literature are reported for thermal neutron energy (25.3 meV) as a standard condition. Considering this, Figure S5 shows a comparison of normalized light yields and pulses per neutron values, vs $^{10}B_5C$ thickness, calculated for the NORMA neutron spectrum and for thermal neutron energy. The light yield is proprotional to the integrated electronic stopping in $Al_2O_3$, while the number of pulses per neutron gives the probablity for α- and Li-entrance[21] into the scintillator irrespective of the extent of kinetic energy carried by the entering particle (here, a lower level discriminator setting[20,21] is not applied). Despite the different definitions, the curves in Figure S5a,b are quite similar. The peak positions slightly differ as they appear at ∼2.5 and ∼3 μm $^{10}B_5C$ thickness in panels (a) and (b). The lower the neutron energy, the stronger the decay of the light yield and pulse number in the large $^{10}B_5C$ thickness range, that is, well beyond the stopping range of the Li- and α-projectiles. This exponential-like decay[20] is determined by neutron absorption in $^{10}B_5C$ according to the Beer–Lambert law. Markedly, the decay strength is an indicator of the neutron energy, especially in the sub-thermal range. Figure S5b shows maximum efficiencies of 0.08 and 0.045 pulses per neutron, for NORMA and for thermal neutrons, respectively. These values can be compared to the neutron detection efficiencies reported in the ∼1–4% range for $^{10}B/Al_2O_3$ structures[26] and for $^{10}B_4C$ or $^{10}B$-based α-voltaic thermal neutron detectors.[20,22]

The schematic view of the neutron irradiation-induced scintillation process is shown in Figure 6. For clarity, the thin Ti layers are not included since they have no considerable impact on the system's functional operation. Figure 6 represents a neutron conversion event for a given depth position of the neutron-absorbing $^{10}B$ isotope and a certain trajectory direction for the emitted reaction products. In a $^{10}B$ fission event, the α- and Li-particles depart in opposite directions along a randomly oriented emission axis. The same as for neutrons, the trajectories of α- and Li-projectiles can be considered as straight lines since the lateral-to-longitudinal projected range ratios are as low as 0.024 for α-particles and 0.058 for Li-particles in $B_5C$, according to SRIM[53] simulations. The violet-colored fraction of the α-particle trajectory in Figure 6 represents electronic stopping in the modified $Al_2O_3$ region where target excitation is accompanied by photon emission from the F and $F^+$ centers. In IL yield calculations (dashed lines in Figure 5a), the electronic energy deposition in $Al_2O_3$ was statistically averaged considering the depth-dependent neutron absorption in $^{10}B_5C$ and random emission direction of the α- and Li-particles in the $^{10}B$ fission events. The number of photons emitted in IL is supposed to be proportional to the total amount of ionization energy deposited in $Al_2O_3$.[54] In the $^{10}B(n,\alpha\gamma)^7Li^*$ reaction, the 470 keV γ-photon is emitted in random directions. Its linear attenuation coefficient is as low as ∼0.1 $cm^{-1}$ in both $^{10}B_5C$ and $Al_2O_3$;[55−57] therefore, the few Compton electrons generated may not induce considerable cathodoluminescence[58] in $Al_2O_3$ when compared to the α- and Li-related ionoluminescence. Recent modeling studies report excellent γ-rejection capabilities for neutron detectors based on a boron carbide absorber atop a thin (∼1–10 μm) semiconductor charge collection layer.[27,28] Similarly, low γ-detection efficiency and related low background can be anticipated for a thin (∼3 μm) $Al_2O_3$ scintillator coupled to a $B_5C$ layer.

Note that an advantage to use $Al_2O_3$ as a scintillator is related to its low average atomic number ($Z$) as it results in short stopping ranges $R_p(He) = 3$ μm and $R_p(Li) = 1.5$ μm for the α- and Li-reaction products (see Figure S3a) compared to those measured in other scintillators, e.g., $Cs_3Cu_2I_5$ perovskites[54] with $R_p(He) = 5.6$ μm and $R_p(Li) = 2.7$ μm or ZnS with $R_p(He) = 4.2$ μm and $R_p(Li) = 2.3$ μm, according to SRIM simulations. Therefore, the coupling of an $Al_2O_3$ scintillator with a $^{10}B_5C$ absorber is favorable when enhanced lateral resolution is required for neutron detection. Moreover, the low-$Z$ of $Al_2O_3$ leads to weak γ-ray absorption that is beneficial when external γ-ray background rejection is important during neutron detection. Other scintillators, which comprise heavier elements,

Downloaded from pubs.acs.org/aaembp/article-pdf/8/19/8664/6858615/el-2026-01505k.pdf by CENTER FOR ENERGY RESEARCH user on 06 November 2026



https://doi.org/10.1021/acsaelm.6c01505
ACS Appl. Electron. Mater. 2026, 8, 8664−8672

like $Cs_3Cu_2I_5$, BGO, or ZnS, show stronger γ-ray absorption and weaker γ-background rejection capability.

Regarding radiation resistance, in α-$Al_2O_3$, the γ-photons can generate Compton electrons with a maximum kinetic energy of ~300 keV while the threshold to generate oxygen atomic displacements is reported in the 240–400 keV range (for a displacement energy range of 41–76 eV).[59,60] One may suppose that the Compton displacement effect does not noticeably change the optical properties of $Al_2O_3$ via the generation of new F and $F^+$ centers or other defects. Although the energetic α- and Li-projectiles may create lattice defects in both $B_5C$ and $Al_2O_3$, considering the applied neutron fluences of $10^9$ to $10^{10}$ $cm^{-2}$, the developing α- and Li-fluences are much lower than those used in ion irradiation experiments for optical defect center production.[32,61] As for comparison, in this work, the modified $Al_2O_3$ zones were created by MeV energy $N^+$ irradiation in the fluence range of ~$10^{13}$ to $10^{15}$ $cm^{-2}$.

The electronic stopping of α- and Li-projectiles in our $B_5C$ material does not result in light production. This was checked by photoluminescence experiments (not shown here) revealing no appreciable light emission from the amorphous $B_5C$ layers. Spectroscopic ellipsometry (SE) measurements were carried out on Si/Ti/$B_5C$ structures to determine the boron carbide dielectric function. A typical example for pseudo $n$ and $k$ spectra can be seen in Figure 7 for a ca. 1150 nm-thick $B_5C$ layer. The evaluated optical absorption depth varies between 25 and 210 nm in the wavelength range of 300–800 nm. This means that besides their weak luminescence capability, the as-deposited $B_5C$ layers are rather opaque. This is expected for the amorphous phase, while for single crystal or polycrystalline ceramic boron carbide, the extinction is weaker, thus giving typical optical penetration depths of several microns.[23] In Figure 7, the refractive index at $\lambda = 633$ nm is $n = 2.78$, being relatively high similarly to what was found by others for boron carbide layers prepared by low power magnetron sputtering at room temperature.[62] Although its optical properties do not predestinate amorphous $^{10}B_5C$ as an effective scintillator, the room temperature deposition of the material requires low thermal budget and its combination with $Al_2O_3$ results in effective scintillation-based neutron detection.

## 4. CONCLUSIONS

We presented a detailed structural and functional characterization of sputter-deposited amorphous $^{10}B_5C$ layers combined with oxygen vacancy-enriched α-$Al_2O_3$ scintillators using proton elastic backscattering spectrometry, scanning electron microscopy, spectroscopic ellipsometry, neutron absorption, and neutron beam-induced scintillation measurements supported by the modeling of ion stopping in the absorber/scintillator structure and the calculation of detector response like the intensity of induced light or the number of counts per neutron. The combination of $^{10}B_5C$ layers with different thicknesses and $Al_2O_3$ crystals containing different amounts of oxygen vacancy-related luminescence centers in their thin near-surface region results in a versatile structure with variable neutron conversion efficiency. The presented observations on cold neutron absorption and neutron-to-light conversion efficiency are all explicable when tracking in detail the energy production and conversion processes in the $^{10}B_5C/Al_2O_3$ system and considering the applied neutron energy spectrum, energy-dependent neutron absorption and scattering effects, and the transfer characteristics of the optical detection line. Based on this concept, reliable process control and optimization of compact, versatile, solid state, boron carbide thin layer-containing device structures for neutron detection or neutron shielding can be realized.

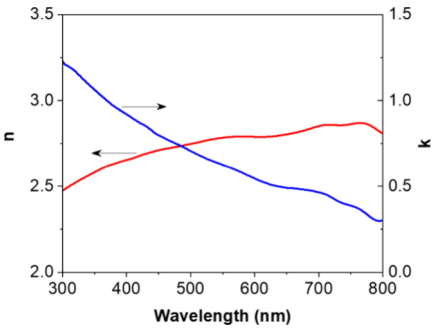



**Figure 7.** Pseudo $n$ and $k$ spectra of a sputter-deposited amorphous $^{10}B_5C$ layer evaluated from spectroscopic ellipsometry measurements.

## ■ ASSOCIATED CONTENT

### Supporting Information

The Supporting Information is available free of charge at https://pubs.acs.org/doi/10.1021/acsaelm.6c01505.

Boron carbide layer thickness data from p-EBS and SEM analysis, neutron transmission light yield maps for bare Si and $Al_2O_3$ substrates, $He^+$- and $Li^+$-induced electronic stopping profiles in boron carbide and in sapphire, 1.5 MeV $He^+$ ion-induced luminescence yield of the F and $F^+$ centers in different $Al_2O_3$ scintillators, and neutron-induced light yield and pulses per neutron values calculated at different neutron energies as a function of boron carbide layer thickness (PDF)

## ■ AUTHOR INFORMATION

### Corresponding Author

**Zsolt Zolnai** – *Institute of Technical Physics and Materials Science, HUN-REN Centre for Energy Research, Konkoly-Thege Miklós út 29-33, Budapest H-1121, Hungary;* orcid.org/0000-0003-3457-7679; Email: zolnai.zsolt@ek.hun-ren.hu

### Authors

**Zoltán Kis** – *Budapest Neutron Centre, Institute for Energy Security and Environmental Safety, HUN-REN Centre for Energy Research, Konkoly-Thege Miklós út 29-33, Budapest H-1121, Hungary*

**Nguyen Quoc Khánh** – *Institute of Technical Physics and Materials Science, HUN-REN Centre for Energy Research, Konkoly-Thege Miklós út 29-33, Budapest H-1121, Hungary*

**Zoltán Kovács** – *Institute of Technical Physics and Materials Science, HUN-REN Centre for Energy Research, Konkoly-Thege Miklós út 29-33, Budapest H-1121, Hungary*

**Péter Petrik** – *Institute of Technical Physics and Materials Science, HUN-REN Centre for Energy Research, Konkoly-Thege Miklós út 29-33, Budapest H-1121, Hungary; Department of Electrical Engineering, University of Debrecen, Bem tér 18, Debrecen H-4026, Hungary*

**Chao Zeng** – *Institute of Technical Physics and Materials Science, HUN-REN Centre for Energy Research, Konkoly-*

Downloaded from pubs.acs.org/aaembp/article-pdf/8/19/8664/6858615/el-2026-01505k.pdf by CENTER FOR ENERGY RESEARCH user on 06 November 2026



https://doi.org/10.1021/acsaelm.6c01505
ACS Appl. Electron. Mater. 2026, 8, 8664–8672

*Thege Miklós út 29-33, Budapest H-1121, Hungary; Doctoral School of Materials Sciences and Technologies, Óbuda University, Tavaszmező u. 17, Budapest H-1084, Hungary*

**Edit Szilágyi** – *Institute for Particle and Nuclear Physics, HUN-REN Wigner Research Centre for Physics, Konkoly-Thege Miklós út 29-33, Budapest H-1121, Hungary*

**Attila Németh** – *Institute for Particle and Nuclear Physics, HUN-REN Wigner Research Centre for Physics, Konkoly-Thege Miklós út 29-33, Budapest H-1121, Hungary*

**László Szentmiklósi** – *Budapest Neutron Centre, Institute for Energy Security and Environmental Safety, HUN-REN Centre for Energy Research, Konkoly-Thege Miklós út 29-33, Budapest H-1121, Hungary*

**János Volk** – *Institute of Technical Physics and Materials Science, HUN-REN Centre for Energy Research, Konkoly-Thege Miklós út 29-33, Budapest H-1121, Hungary*

Complete contact information is available at: https://pubs.acs.org/doi/10.1021/acsaelm.6c01505

### Author Contributions

CRediT authorship contribution statement **Z. Zolnai**: conceptualization, methodology, investigation, and writing–original draft. **Z. Kis**: conceptualization, methodology, investigation, and writing–review and editing. **N. Q. Khánh**, **P. Petrik**, and **J. Volk**: methodology and writing–review and editing. **Z. Kovács**: investigation, data curation, and writing–review and editing. **C. Zeng**: investigation and data curation. **E. Szilágyi**: investigation and writing–review and editing. **A. Németh**: investigation. **L. Szentmiklósi**: methodology.

### Notes

The authors declare no competing financial interest.

## ■ ACKNOWLEDGMENTS

The authors would like to thank the reactor operations staff at the Budapest Neutron Centre and the accelerator operations staff at the HUN-REN Wigner Research Centre for Physics. Kind help from V. Szilágyi and M. Gracheva during NORMA measurements is highly appreciated. This work received funding from the NRDI Fund of Hungary under grants K-143263 and K-146181. Project nos. TKP2021-NVA-03 and TKP2021-EGA-04 have been implemented with the support provided by the Ministry of Innovation and Technology of Hungary from the National Research, Development and Innovation Fund (NRDI), financed under the TKP2021 funding scheme. The development of the NORMA facility was supported by project no. RRF-2.3.1-21-2022-00009, titled National Laboratory for Renewable Energy, that has been implemented with the support provided by the Recovery and Resilience Facility of the European Union within the framework of Programme Széchenyi Plan Plus.

## ■ REFERENCES

(1) Staf, H.; Kis, Z.; Szentmiklósi, L.; Kaplan, B.; Olsson, E.; Larsson, P.-L. Determining the density distribution in cemented carbide powder compacts using 3D neutron imaging. *Powder Technol.* **2019**,*354*, 584–590.

(2) Szentmiklósi, L.; Maróti, B.; Kis, Z. Quantitative, non-destructive elemental composition analysis of 3D-structured samples. *J. Anal. At. Spectrom.* **2023**, *38*, 333–341.

(3) Bozzini, B.; Cazzanti, S.; Hippoliti, R.; Kis, Z.; Rovatti, L.; Tavola, F. Non-destructive analysis of Pb-acid battery positive plates, based on neutron tomography. *JPhys Energy* **2024**, *6*, No. 015006.

(4) Skalden, J.; Ehresmann, M.; Becatti, G.; Schulz, M.; Gustschin, A.; Kornmeier, J. R.; Kis, Z.; Szentmiklósi, L.; Herdrich, G. Neutron imaging investigation of additively manufactured tungsten nozzles for an arcjet deorbit system. *J. Electr. Propuls.* **2025**, *4* (1), 52.

(5) Piscitelli, F.; Messi, F.; Anastasopoulos, M.; Brys, T.; Chicken, F.; Dian, E.; Fuzi, J.; Höglund, C.; Kiss, G.; Orban, J.; Pazmandi, P.; Robinson, L.; Rosta, L.; Schmidt, S.; Varga, D.; Zsiros, T.; Hall-Wilton, R. The Multi-Blade Boron-10-based neutron detector for high intensity neutron reflectometry at ESS. *J. Instrum.* **2017**, *12*, No. P03013.

(6) Dankowski, J.; Bielecki, J.; Błądek, J.; Conroy, S.; Coriton, B.; Croci, G.; Dworaka, D.; Ericsson, G.; Eriksson, J.; Wójcik-Gargula, A.; Hjalmarsson, A.; Jardin, A.; Kantor, R.; Kovalev, A.; Król, K.; Kulińska, A.; Kurowski, A.; Mariano, G.; Mehrara, R.; Morawski, D.; Rebai, M.; Scholz, M.; Scioscioli, F.; Tardocchi, M.; Tracz, G.; Turzański, M.; Wiącek, U. Development and performance of the thin-foil proton recoil spectrometer for ITER plasma diagnostics. *Fusion Eng. Des.* **2025**, *219*, No. 115263.

(7) Platow, W.; Rubin, L.; Mayfield, P.; Lessard, R.; Whalen, P.; Roberge, S. Neutron radiation due to high energy boron ion beams. *MRS Adv.* **2022**, *7*, 1476–1481.

(8) Turcaud, J. A.; Heckman, C.; Heckman, V.; Hassan, A.; Pong, R.; Schuur, J. Risk of neutron generation with implantation of light ions. *MRS Adv.* **2022**, *7*, 1343–1346.

(9) Stevanato, L.; Baroni, G.; Cohen, Y.; Fontana, C. L.; Gatto, S.; Lunardon, M.; Marinello, F.; Moretto, S.; Morselli, L. A Novel Cosmic-Ray Neutron Sensor for Soil Moisture Estimation over Large Areas. *Agriculture* **2019**, *9*, No. 202.

(10) Brall, T.; Mares, V.; Bütikofer, R.; Rühm, W. Assessment of secondary neutrons from galactic cosmic rays at mountain altitudes – Geant4 simulations and ground-based measurements of neutron energy spectra. *Radiat. Meas.* **2021**, *144*, No. 106592.

(11) Shah, G. N.; Razdan, H.; Bhat, C. L.; Ali, Q. M. Neutron generation in lightning bolts. *Nature* **1985**, *313*, 773.

(12) Toropov, A. A.; Kozlov, V. I.; Mullayarov, V. A.; Starodubtsev, S. A. Experimental observations of strengthening the neutron flux during negative lightning discharges of thunderclouds with tripolar configuration. *J. Atmos. Sol.-Terr. Phys.* **2013**, *94*, 13–18.

(13) Stenkin, Y.; Alekseenko, V.; Cai, Z.; Cao, Z.; Cattaneo, C.; Cui, S.; Firstov, P.; Giroletti, E.; Guo, X.; He, H.; Liu, Y.; Mad, X.; Shchegolev, O.; Vallania, P.; Vigorito, C.; Yanin, Y.; Zhao, J. Response of the environmental thermal neutron flux to earthquakes. *J. Environ. Radioact.* **2019**, *208-209*, 105981.

(14) Filgas, R.; Malich, M.; Pospíšil, S.; Bergmann, B.; Slavíček, T.; Calzada-Diaz, A. Miniature semiconductor neutron spectrometer HardPix for surface mapping of lunar water, *Acta Astronaut.* **2022**, *200*, 620–625.

(15) Claps, G.; Murtas, F.; Pietropaolo, A.; Celentano, G.; Vannozzi, A.; Santoni, A.; Quintieri, L.; Riedel, R. A. $^{3}$He-free triple GEM thermal neutron detector. *Europhys. Lett.* **2014**, *105*, No. 22002.

(16) Mirenda, M.; Rodrigues, D.; Arenillas, P.; Gutkowski, K. Ionic liquids as solvents for liquid scintillation technology. Čerenkov counting with 1-Butyl-3-Methylimidazolium Chloride. *Radiat. Phys. Chem.* **2014**, *98*, 98–102.

(17) Zeitelhack, K. Search for alternative techniques to helium-3 based detectors for neutron scattering applications. *Neutron News* **2012**, *23*, 10–13.

(18) Chuirazzi, W.; Craft, A.; Schillinger, B.; Cool, S.; Tengattini, A., Boron-Based Neutron Scintillator Screens for Neutron Imaging. *J. Imaging* **2020**, *6*, No. 124.

(19) Schillinger, B.; Chuirazzi, W.; Cool, S.; Craft, A.; Kis, Z.; Szentmiklósi, L.; Tengattini, A. New Measurements on Borated Neutron Imaging Screens at Budapest Neutron Centre (BNC). *J. Phys.: Conf. Ser.* **2023**, *2605*, No. 012009.

(20) McGregor, D. S.; Hammig, M. D.; Yang, Y.-H.; Gersch, H. K.; Klann, R. T. Design considerations for thin film coated semiconductor thermal neutron detectors—I: basics regarding alpha particle emitting neutron reactive films. *Nucl. Instrum. Methods Phys. Res. A*, **2003**, *500*, 272–308.

Downloaded from pubs.acs.org/aaembp/article-pdf/8/19/8664/6858615/el-2026-01505k.pdf by CENTER FOR ENERGY RESEARCH user on 06 November 2026

(21) McGregor, D. S.; Klann, R. T.; Gersch, H. K.; Yang, Y.-H. Thin-film-coated bulk GaAs detectors for thermal and fast neutron measurements, *Nucl. Instrum. Methods Phys. Res. A* **2001**, *466*, 126–141.
(22) Chaudhari, P.; Singh, A.; Topkar, A.; Dusane, R. Fabrication and characterization of silicon based thermal neutron detector with hot wire chemical vapor deposited boron carbide converter. *Nucl. Instrum. Methods Phys. Res. A*, **2015**, *779*, 33–38.
(23) Domnich, V.; Reynaud, S.; Haber, R. A.; Chhowalla, M. Boron Carbide: Structure, Properties, and Stability under Stress. *J. Am. Ceram. Soc.* **2011**, *94*, 3605–3628.
(24) Höglund, C.; Zeitelhack, K.; Kudejova, P.; Jensen, J.; Greczynski, G.; Lu, J.; Hultman, L.; Birch, J.; Hall-Wilton, R. Stability of $^{10}B_4C$ thin films under neutron radiation. *Radiat. Phys. Chem.* **2015**, *113*, 14–19.
(25) Echeverria, E.; Dong, B.; Peterson, G.; Silva, J. P.; Wilson, E. R.; Driver, M. S.; Jun, Y.-Si; Stucky, G. D.; Knight, S.; Hofmann, T.; Han, Z.-K.; Shao, N.; Gao, Y.; Mei, W.-N.; Nastasi, M.; Dowben, P. A.; Kelber, J. A. Semiconducting boron carbides with better charge extraction through the addition of pyridine moieties. *J. Phys. D: Appl. Phys.* **2016**, *49*, No. 355302.
(26) Celentano, G.; Vannozzi, A.; Mancini, A.; Santoni, A.; Pietropaolo, A.; Claps, G.; Bemporad, E.; Renzelli, M.; Murtas, F.; Quintieri, L. $^{10}B$ enriched film deposited by e-beam technique on $Al_2O_3$ substrate for high efficiency thermal neutron detector. *Surf. Coat. Technol.* **2015**, *265*, 160–165.
(27) Murphy, J. W.; Kunnen, G. R.; Mejia, I.; Quevedo-Lopez, M. A.; Allee, D.; Gnade, B. Optimizing diode thickness for thin-film solid state thermal neutron detectors. *Appl. Phys. Lett.* **2012**, *101*, No. 143506.
(28) Zhang, Z.; Aspinall, M. D. Comparison of Neutron Detection Performance of Four Thin-Film Semiconductor Neutron Detectors Based on Geant4. *Sensors* **2021**, *21*, No. 7930.
(29) Nguyen, L. Q.; Gabella, G.; Goldblum, B. L.; Laplace, T. A.; Carlson, J. S.; Brubaker, E.; Feng, P. L. Boron-loaded organic glass scintillators, *Nucl. Instrum. Methods. Phys. Res. A* **2021**, *988*, No. 164898.
(30) Vu, D.; Dettmann, M.; Herrig, V.; Jacobsohn, L. G.; Kielty, M. W.; Wetzel, J.; Onel, Y.; Akgun, U. A. Neutron Detector Based on Boron-10 Enriched Scintillating Glasses. In *Additive Manufacturing and Strategic Technologies in Advanced Ceramics*, Shimamura, K.; Kirihara, S.; Akedo, J.; Ohji, T.; Naito, M., Ed.; The American Ceramic Society, **2016**, 57–68.
(31) Akselrod, G. M.; Akselrod, M. S.; Benton, E. R.; Yasuda, N. A novel $Al_2O_3$ fluorescent nuclear track detector for heavy charged particles and neutrons. *Nucl. Instrum. Methods Phys. Res. B* **2006**, *247*, 295–306.
(32) Zolnai, Z.; Pal, M. K.; Kótai, E.; Szilágyi, E. Helium ion beam-induced luminescence from defect centers in $Al_2O_3$, In *Proceedings of the Symposium on Materials Science, Mátraháza, Hungary*, Fried, M., Ed., Óbuda University, **2024**, 25–26 ISBN 978-963-449-353-2.
(33) Brewer, J. D.; Jeffries, B. T.; Summers, G. P. Low-temperature fluorescence in sapphire. *Phys. Rev. B* **1980**, *22*, No. 4900.
(34) Evans, B. D.; Stapelbroek, M. Optical properties of the $F^+$ center in crystalline $Al_2O_3$. *Phys. Rev. B* **1978**, *18*, No. 7089.
(35) Szilágyi, E.; Pal, M. K.; Kótai, E.; Zolnai, Z.; Bányász, I. Fluence evolution of defects in α-$SiO_2$ determined by ionoluminescence. *Nucl. Instrum. Methods. Phys. Res. B* **2024**, *555*, No. 165470.
(36) Pászti, F.; Manuaba, A.; Hajdu, C.; Melo, A. A.; Da Silva, M. F. Current measurement on MeV energy ion beams. *Nucl. Instrum. Methods Phys. Res. B* **1990**, *47*, 187.
(37) Kótai, E. Computer methods for analysis and simulation of RBS and ERDA spectra. *Nucl. Instrum. Methods Phys. Res. B* **1994**, *85*, 588.
(38) Mazzoni, S.; Chiari, M.; Giuntini, L.; Mandó, P. A.; Taccetti, N. Proton elastic scattering cross section on carbon from 350 keV to 3 MeV. *Nucl. Instrum. Methods Phys. Res. B* **1998**, *136-138*, 86.
(39) Chiari, M.; Giuntini, L.; Mandó, P. A.; Taccetti, N. Proton elastic scattering cross-section on boron from 0.5 to 3.3 MeV. *Nucl. Instrum. Methods Phys. Res. B* **2001**, *184*, 309.
(40) Ion Beam Analysis Nuclear Data Library (IBANDL), https://www-nds.iaea.org/exfor/ibandl.htm.
(41) Zolnai, Z.; Toporkov, M.; Volk, J.; Demchenko, D. O.; Okur, S.; Szabó, Z.; Özgür, Ü.; Morkoc, H.; Avrutin, V.; Kótai, E. Nondestructive atomic compositional analysis of BeMgZnO quaternary alloys using ion beam analytical techniques, *Appl. Surf. Sci.* **2015**, *327*, 43–50.
(42) Zolnai, Z.; Petrik, P.; Németh, A.; Volk, J.; Bosi, M.; Seravalli, L.; Fornari, R. Atomic structure and annealing-induced reordering of ε-$Ga_2O_3$: a Rutherford Backscattering/Channeling and Spectroscopic Ellipsometry study. *Appl. Surf. Sci.* **2023**, *636*, No. 157869.
(43) Khánh, N. Q.; Horváth, Z. E.; Zolnai, Z.; Petrik, P.; Pósa, L.; Volk, J. Effect of process parameters on co-sputtered $Al_{(1-x)}Sc_xN$ layer's properties: Morphology, crystal structure, strain, band gap, and piezoelectricity. *Mat. Sci. Semicon. Proc.* **2024**, *169*, No. 107902.
(44) Bosio, A.; Parisini, A.; Lamperti, A.; Borelli, C.; Fornasini, L.; Bosi, M.; Cora, I.; Fogarassy, Z.; Pécz, B.; Zolnai, Z.; Németh, A.; Vantaggio, S.; Fornari, R. n-Type doping of ε-$Ga_2O_3$ epilayers by high-temperature tin diffusion, *Acta Mater.* **2021**, *210*, No. 116848.
(45) Hegedüs, N.; Lovics, R.; Serényi, M.; Zolnai, Z.; Petrik, P.; Balázsi, C.; Balázsi, K. Interpretation of hydrogen incorporation into radio frequency sputtered amorphous silicon based on Berg modelling. *Vacuum* **2022**, *202*, No. 111164.
(46) Lábadi, Z.; Takács, D.; Zolnai, Z.; Petrik, P.; Fried, M. Compositional Optimization of Sputtered $WO_3/MoO_3$ Films for High Coloration Efficiency. *Materials* **2024**, *17* (5), No. 1000.
(47) Gajdics, M.; Cora, I.; Kolonits, T.; Sáfrán, G.; Szilágyi, E.; Zolnai, Z.; Pécz, B. Composition-dependent structural and optical properties of combinatorially deposited, RF sputtered gallium oxynitride layers. *Vacuum* **2026**, *247*, No. 115133.
(48) Kis, Z. The redesigned neutron imaging facility, NORMA at BNC, *Budapest. Rev. Sci. Instrum.* **2024**, *95* (7), No. 073702.
(49) NORMA, Budapest Neutron Centre (BNC), https://bnc.hu/norma/.
(50) Chu, W-K.; Mayer, J. W.; Nicolet, M. A. *Backscattering Spectrometry*, Academic Press: New York, **1978**, ISBN 0-12-173850-7
(51) Sears, V. F. Neutron scattering lengths and cross sections. *Neutron News* **1992**, *3*, 26–37.
(52) Gokul, P.; Kumar, J. A.; Preetha, R.; Chattopadhyaya, S.; Basu, P.; Menaka, M.; Subramanian, V.; Venkatraman, B.; Sathyan, D.; Jayanarayanan, K.; Madhavan, M. K. Development of boron carbide concrete for enhanced radiation shielding in nuclear reactors. Case Stud. *Constr. Mater.* **2025**, *22*, No. e04354.
(53) Computer simulation of the Stopping and Range of Ions in Matter (SRIM), http://www.srim.org.
(54) Hunyadi, M.; Samu, G. F.; Csige, L.; Csík, A.; Buga, C.; Janáky, C. Scintillator of Polycrystalline Perovskites for High-Sensitivity Detection of Charged-Particle Radiations. *Adv. Funct. Mater.* **2022**, *32*, No. 2206645.
(55) Buyuk, B; Tugrul, A. B. Gamma and neutron attenuation behaviours of boron carbide–silicon carbide composites. *Ann. Nucl. Energy* **2014**, *71*, 46–51.
(56) Tekin, H. O.; Altunsoy, E. E.; Ozturk, F. C.; Kilicoglu, O.; Sayyed, M. I. Gamma-Ray Attenuation Properties of Boron Carbide in Radiological Energy Range Using MCNPX Code. *AIP Conf. Proc.* **2018**, *2042*, No. 020059.
(57) Zaim, N.; Bayhatun, O. A Study on the Gamma-Ray Attenuation Coefficients of $Al_2O_3$ and $Al_2O_3$:$TiO_2$ Compounds. *SDU J. Nat. Appl. Sci.* **2018**, *22*, 312.
(58) Ghamnia, M.; Jardin, C.; Bouslama, M. Luminescent centres F and $F^+$ in α-alumina detected by cathodoluminescence technique. *J. Electron Spectrosc. Relat. Phenom.* **2003**, *133*, 55–63.
(59) Das, G. Determination of the threshold displacement energy in α-$AI_2O_3$ by high voltage electron microscopy. *J. Mater. Sci. Lett.* **1983**, *2*, 453–456.
(60) Pells, G. P.; Stathopoulos, A. Y. Radiation damage in the cation sublattice of α-$AI_2O_3$. *Radiat. Eff.* **1983**, *74*, 181–191.
(61) Crespillo, M. L.; Graham, J. T.; Zhang, Y.; Weber, W. J. In-situ luminescence monitoring of ion-induced damage evolution in $SiO_2$ and $Al_2O_3$. *J. Lumin.* **2016**, *172*, 208–218.
(62) Sulyaeva, V.; Khomyakov, M.; Kosinova, M. Room-Temperature Formation of Hard $BC_x$ Films by Low Power Magnetron Sputtering. *Appl. Sci.* **2021**, *11*, No. 9896.

Downloaded from pubs.acs.org/aaemp/article-pdf/8/19/8664/6858615/el-2026-01505k.pdf by CENTER FOR ENERGY RESEARCH user on 06 November 2026


https://doi.org/10.1021/acsaelm.6c01505
*ACS Appl. Electron. Mater.* 2026, 8, 8664–8672